COMMUNICATION

ADVANCED
ENERGY
MATERIALS

Capacitors

www.advenergymat.de

Synthesis of Pseudocapacitive Polymer Chain Anode and Subnanoscale Metal Oxide Cathode for Aqueous Hybrid Capacitors Enabling High Energy and Power Densities along with Long Cycle Life

Il Woo Ock, Jae Won Choi, Hyung Mo Jeong,* and Jeung Ku Kang*

Aqueous electrochemical energy storages are of enormous attention due to their high safety and being environmentally friendly, but they must satisfy very challenging standards in energy and power densities over long repeated charging/discharging cycles. Herein, a strategy to realize high-performance aqueous hybrid capacitors (AHCs) using pseudocapacitive negative and positive electrodes is reported. Polymer chains, which are synthesized by in situ polymerization of polyaniline on reduced graphene sheets, show fiber-like morphologies and the redox-reactive surface area allowing high capacitance as anode materials even at a high current density of 20 A g^{-1} and a high loading of $\approx$6 mg cm^{-2}. Additionally, subnanoscale metal oxide particles on graphene are utilized as pseudocapacitive cathode materials and they show the approximately threefold higher capacitance than nanocrystals of $\approx$10 nm. Assembling these polymer chain anode and subnanoscale metal oxide cathode in full-cell AHCs is shown to give the high energy density exceeding those of aqueous batteries along with the $\approx$100% capacity retention over 100 000 redox cycles. Additionally, AHCs exhibit the high power density allowing ultrafast charging, so that the switching wearable display kit with two AHCs in series can be charged within several seconds by the flexible photovoltaic module and USB switching charger.

Nowadays, an electrochemical energy storage system (ESS) is an essential part of many applications from portable devices to electrical vehicles. However, the currently dominating ESS remains on lithium-ion batteries operating in environmentally toxic and flammable organic solvents to ensure high voltages for good energy densities, but they still suffer from low power density and slow charging capability.[1,2] Aqueous capacitors, began with electric double-layer capacitors (EDLCs) using porous carbon materials,[3,4] have been developed to overcome these fundamental problems and lead to a battery-type pseudocapacitor that stores ions using redox reactions.[3,5] EDLC-type carbon materials allow low ion absorption/desorption capacity in their electrical double layers. Meanwhile, a metal oxide could be one of promising candidates to realize the positive electrode for atom-by-ion redox reactions, but fast charging/discharging does not enable to achieve its full capacitance. Moreover, a metal oxide typically suffers from long ion diffusion lengths and poor electrical conductivity during redox reactions. This in turn leads to fast fading of capacity, thus resulting in short cycle life.[6,7] Realizing metal oxide particles at several nanometer-scale sizes has been suggested as one of promising solutions to shorten a diffusion length. The problem is in that particles at nanometer scale sizes could be agglomerated during repeated redox cycles, thus eventually causing the capacity fading during repeated charging/discharging cycles. Accordingly, a new electrode architecture or methodology that enables prevention of the agglomeration of electrode materials would allow to give robust capacity retention during repeated charging/discharging cycles. Also, the poor electrical conductivity of pristine metal oxide materials[6,8,9] could be alleviated by their combination with an electrically conducting substrate. Moreover, environmentally safe and low-cost aqueous hybrid capacitors (AHCs) composed of two different negative and positive electrode materials could allow to have a good operation potential window suitable for achieving high energy density.[10] However, most of AHCs were focused on improving the specific capacitances of their positive electrodes since very few pseudocapacitive materials were developed as negative electrodes.[11] Consequently, the strategy to realize high energy and power densities along with long cycle life for AHCs is still very challenging due to loss in the capacity

I. W. Ock, J. W. Choi, Prof. J. K. Kang
Graduate School of Energy
Environment
Water and Sustainability (EEWS)
Korea Advanced Institute of Science and Technology (KAIST)
291 Daehak-ro, Yuseong-gu, Daejeon 34141, Republic of Korea
E-mail: jeungku@kaist.ac.kr
Prof. H. M. Jeong
Department of Nano Applied Engineering
Kangwon National University
1 Kangwondaehak-gil, Chuncheon-si, Gangwon-do 24341
Republic of Korea
E-mail: hmjeong704@kangwon.ac.kr

**ADVANCED
SCIENCE NEWS**
www.advancedsciencenews.com

**ADVANCED
ENERGY
MATERIALS**
www.advenergymat.de

of the negative electrode material along with the fading capacity of the positive electrode during repeated redox cycles.[12]

Herein, we demonstrate high-performance AHCs on a new paradigm architecture for pseudocapacitive negative and positive electrodes, where polymer chains and subnanoscale metal oxide pseudocapacitive materials have been employed as negative and positive electrodes for a hybrid capacitor in the environmentally friendly and safe aqueous electrolyte. Indeed, assembling the negative electrode with the positive electrode is shown to exhibit the high energy density equivalent to those of aqueous batteries, together with excellent capacity retention over long cycle life of 100 000 charging/discharging cycles and ultrafast charging capability enabled by the nearly 100-fold higher power density than those of aqueous batteries.

Figure 1a,b shows a schematic diagram for synthetic methods of anode and cathode pseudocapacitive materials along with a strategy integrating both of anode and cathode structures in the aqueous electrolyte (KOH) for excellent electrochemical performance. The anode materials have been synthesized by in situ polymerization into homogeneously dispersed polymer chains on reduced graphene oxide (rGO) sheets, where polyaniline (PANI) chains act as redox-reactive sites for cations (Figure 1c). Details for the in situ polymerization of PANI chains on rGO sheets are described in the Experimental section (Supporting Information). The transmission electron microscopy (TEM) image shows the morphology of the homogeneously dispersed PANI on the rGO substrate and it is notable that the interaction of PANI with the rGO by π–π conjugation[13,14] could help formation of an electrically conductive network. Furthermore, reducing[15,16] nickel oxide (NiO) nanoparticles of $\approx$10 nm to subnanoscale sizes on the rGO substrate are exhibited to result in large active sites for anions for atom-by-ion redox reactions (Figure 1d). Additionally, AHCs configured on two different anode and cathode materials could achieve a wide operational potential.

PANI morphologies showed the distinct differences as confirmed by TEM and scanning transmission electron microscopy
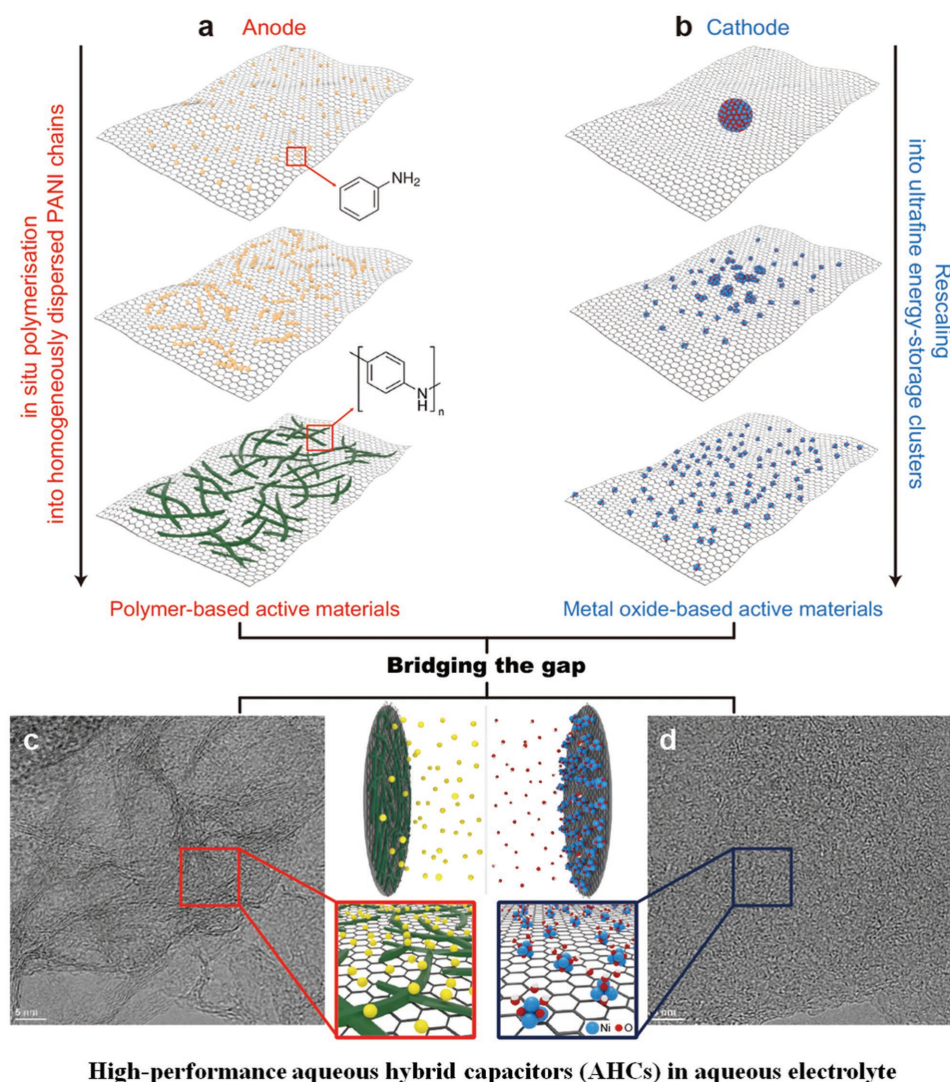

Figure 1. Schematic diagram for synthetic methods of a) polymer chains based negative electrode material (PANI$_x$/rGO) and b) subnanoscale metal oxides based positive electrode material (rescaled NiO/rGO). Schematic mechanisms and TEM images of c) PANI$_{12.5}$/rGO for the anode and d) rescaled NiO/rGO for the cathode in a full-cell AHC.
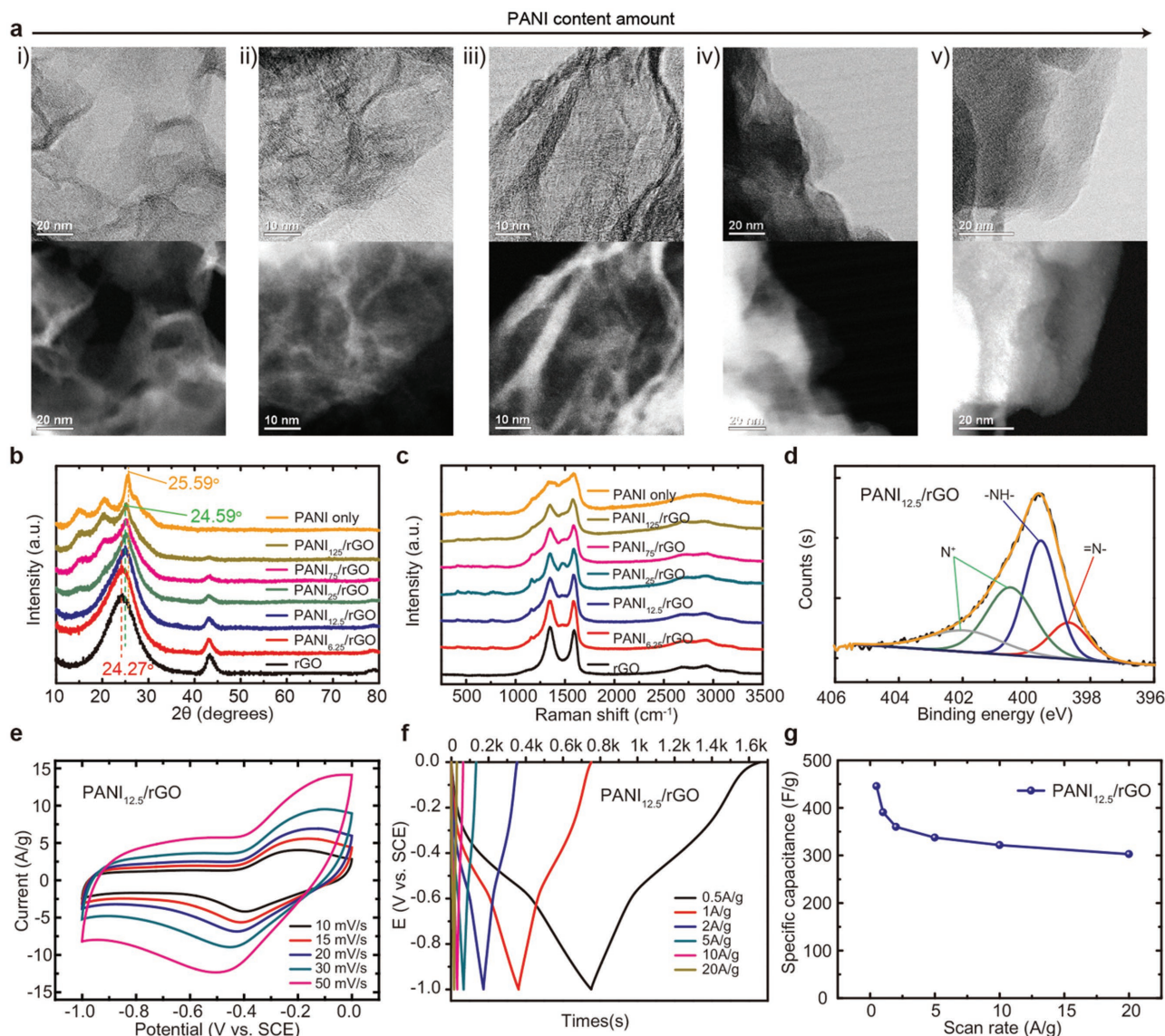
ADVANCED
SCIENCE NEWS
www.advancedsciencenews.com

ADVANCED
ENERGY
MATERIALS
www.advenergymat.de

Figure 2. Characterization of PANI$_x$/rGO versus the amounts of PANI chains: a) TEM and STEM images of i) $x = 6.25$, ii) $x = 12.5$, iii) $x = 25$, iv) $x = 75$, and v) $x = 125$, b) PXRD patterns, c) Raman spectra with $\lambda = 514$ nm, and d) XPS N1s spectra. Electrochemical performance of the optimized anode (PANI$_{12.5}$/rGO): e) CV curves, f) galvanostatic charge–discharge measurements, and g) gravimetric specific capacitances.

(STEM) images (**Figure 2**a; Figure S1, Supporting Information). In the case of PANI$_x$/rGO composites with $x = 6.25$, 12.5, and 25 (Figure 2ai–iii; Figure S1a–c, Supporting Information), the net-like fibers are cross-linked on the rGO surfaces and the widths of fiber-like PANIs are in the range of 2–4 nm for $x = 6.25$ and 12.5 and 5–7 nm for $x = 25$. Meanwhile, for $x = 75$ and 125 (Figure 2aiv,v; Figure S1d,e, Supporting Information), plate-shaped PANIs are formed on the rGO. The powder X-ray diffraction (PXRD) patterns of PANI$_x$/rGO in Figure 2b show that 23.7° and 43° peaks correspond to the (002) and (100) planes of pure rGO, while 15.1°, 20.4°, and 25.2° peaks match with (011), (020), and (200) planes of PANIs in an emeraldine salt form, respectively.[17,18] During formation of PANI$_x$/rGO, the peak at 25.2° is shown to be shifted into 24.2–24.7° attributed to the closer packing of the PANI chains on rGO

layers. Furthermore, the peak intensity of PANI$_x$/rGO composites indicates the π–π interchain interactions between PANI chains. Raman spectra for PANI$_x$/rGO (Figure 2c) confirm the interaction between PANI and rGO. As the amount of PANI is decreased in the PANI$_x$/rGO composite, the 1587 cm^{-1} peak has been blue-shifted, while the 1341 cm^{-1} peak is red-shifted (Figure S2, Supporting Information). The Raman shift is caused by the π–π conjugation[19,20] between PANI and rGO. Moreover, the X-ray photoelectron spectroscopy (XPS) N1s spectra (Figure 2d; Figure S3 and Table S1, Supporting Information) are compared for PANI$_x$/rGO composites. As the PANI chains are increased, the total atomic weight percent of nitrogen is increased from 3.57 to 10.68 at%. The XPS N1s peak is separated by imine nitrogen (=N−), amine nitrogen (−NH−), and positively charged nitrogen (N$^+$: oxidized amine
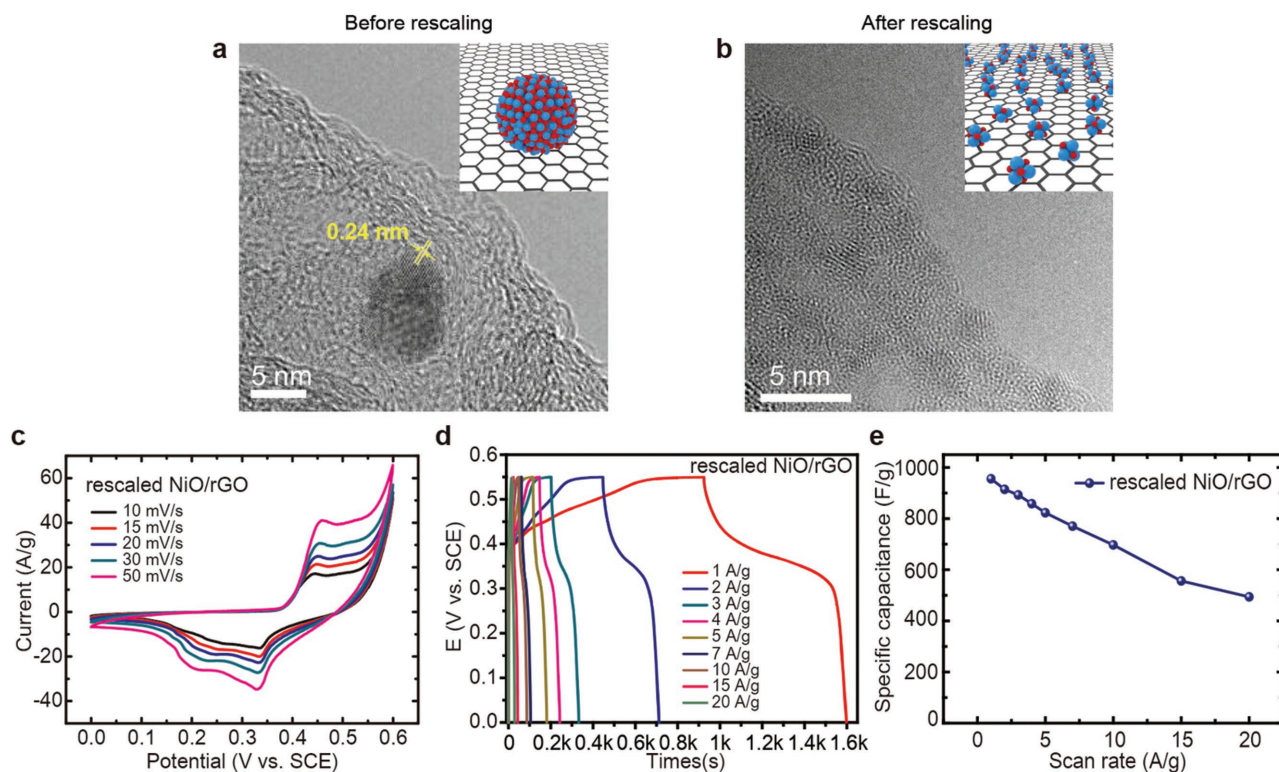
Figure 3. TEM characterization of a) the single NiO nanoparticle attached on rGO and b) the morphology after lithiation-induced rescaling, where images of NiO particles before and after rescaling have been obtained at the same position. Electrochemical performance of optimized cathode (rescaled NiO/rGO): c) CV curves, d) galvanostatic charge–discharge measurements, and e) gravimetric specific capacitances.

and protonated imine).[21,22] The good conductivity is achieved at higher nitrogen doping levels of N+/N, so that XPS N1s peak spectra give clues for electrical performances.[23,24] The PANI$_x$/rGO composite has the highest N doping level at $x = 12.5$ equivalent to the ratio of 0.33 for =N−/−NH−, matching with the imine:amine ratio of 1:3. The results show that a good electrical conductivity could be obtained with $x = 6.25–25$. Meanwhile, in cases of $x = 75–125$ where the =N−/−NH− value increases and PANI shows a plate morphology, amines and imines are oxidized and act as defect sites thus leading to the decrease of conductivity. These results clarify that the ratio of aniline to oxidant in the formation of PANI polymers plays as a descriptor to determine their morphologies and electrical conductance.

The electrochemical properties of PANI$_x$/rGO electrode have also been measured in a three-electrode system in a 6 M KOH aqueous electrolyte. Cyclic voltammetry (CV) curves show a broad pair of redox peaks at the range of anodic potential from −1 to 0 V. This supports that the PANI$_x$/rGO composite is a pseudocapacitive anode material with a high operation voltage (Figure 2e; Figure S4, Supporting Information). The shape of the CV curve is determined to be maintained with a high scan rate of 50 mV s^{-1}, demonstrating that the fast Faradic reaction and efficient charge transfer occurs in the anode system.[25] Galvanostatic charge–discharge measurements (Figure 2f,g; Figure S5 and Table S2, Supporting Information) at the current density of 1 A g^{-1} have given the specific capacitance of 390.7 F g^{-1} at $x = 12.5$. In the case of $x = 12.5$, the specific capacitances of 445.7 F g^{-1} at 0.5 A g^{-1} and 302.8 F g^{-1} at a high

current density of 20 A g^{-1} are shown to exceed those of other reported redox-reactive anode materials in aqueous electrolyte.[26–29] Fiber-type PANI structures have a large surface area and give enhanced charge-transport properties by various factors such as a morphology,[18] interaction with rGO surfaces,[20] and N contents.[23] Indeed, we find that the π–π conjugation of PANI with the rGO and the highest value of nitrogen doping level (N+/N ≈ 0.38, Table S1, supporting information) provide high conductivity for electrons and redox ions, thereby leading to highly improved electrochemical performance. Also, electrochemical performances of PANI$_{12.5}$/rGO anodes on different mass loadings of 0.879, 1.780, and 5.372 mg cm^{-2} at the current density of 1 A g^{-1} (Figure S6, Supporting Information) show that the capacitance of 300 F g^{-1} at the highest mass loading is only about 25% less compared to that on the lower mass loading by about sixfold. This signals that PANI$_{12.5}$/rGO composites of varying mass loading levels could be designed as high-performance anodes for various full-cell energy storage devices.

Furthermore, we have investigated structures and electrochemical performance on the size tuning of NiO. **Figure 3** shows the morphology change of NiO nanoparticles on the rGO substrate. Nanoparticles are at an average size of 10 nm adhered to the rGO sheet (Figure 3a) and PXRD patterns (Figure S7a, Supporting Information) show that they are in a NiO phase. The PXRD peaks at 36.8°, 42.9°, and 62.9° are for (111), (200), and (220) planes.[16,30] Meanwhile, PXRD patterns of subnanoscale NiO particles are not clearly distinguished by

**ADVANCED
SCIENCE NEWS**

www.advancedsciencenews.com

**ADVANCED
ENERGY
MATERIALS**

www.advenergymat.de

extremely small sizes of particles (Figure 3b; Figure S7a, Supporting Information).[31,32] The gravimetric weight percentages (Figure S7b, Supporting Information) of NiO particles before and after rescaling have also been determined through the thermogravimetric analysis. Moreover, the XPS C1s and O1s spectra (Figure S8, Supporting Information) give the information for NiO bonding with the rGO. The XPS C1s spectra for C−OH/C−ONi and the XPS O1s spectra for C−O−Ni are shown to be increased after rescaling, while the XPS O1s spectra for Ni−O are decreased. These demonstrate that NiO binds with the rGO via the C−O−Ni linkage[33] and the C−O−Ni linkages between NiO particles and the rGO after rescaling are increased.. The STEM mapping image (Figure S9, Supporting Information) also clarifies that nanocrystals of ≈10 nm have

been rescaled largely into subnanoscale NiO particles less than 1 nm. Fe_2O_3 and MnO_2 particles have also been observed to be rescaled into subnanoscale sizes on the rGO by adopting the rescaling process for NiO/rGO. These results imply that the rescaling process could be generally applied to realize subnanoscale particles from various metal oxide nanoclusters (Figure S10, Supporting Information). Moreover, the electrochemical anion-storing properties were evaluated in a three-electrode system with 6 M KOH aqueous media (Figure 3c–e; Figure S9, Supporting Information). The CV curves show a pair of redox peaks identifying as NiO particles[16,30] at the range of potential 0–0.6 V (Figure 3c). The subnanoscale NiO/rGO had an increased current density compared to a pristine NiO/rGO (Figure S11a, Supporting Information) and a broader redox
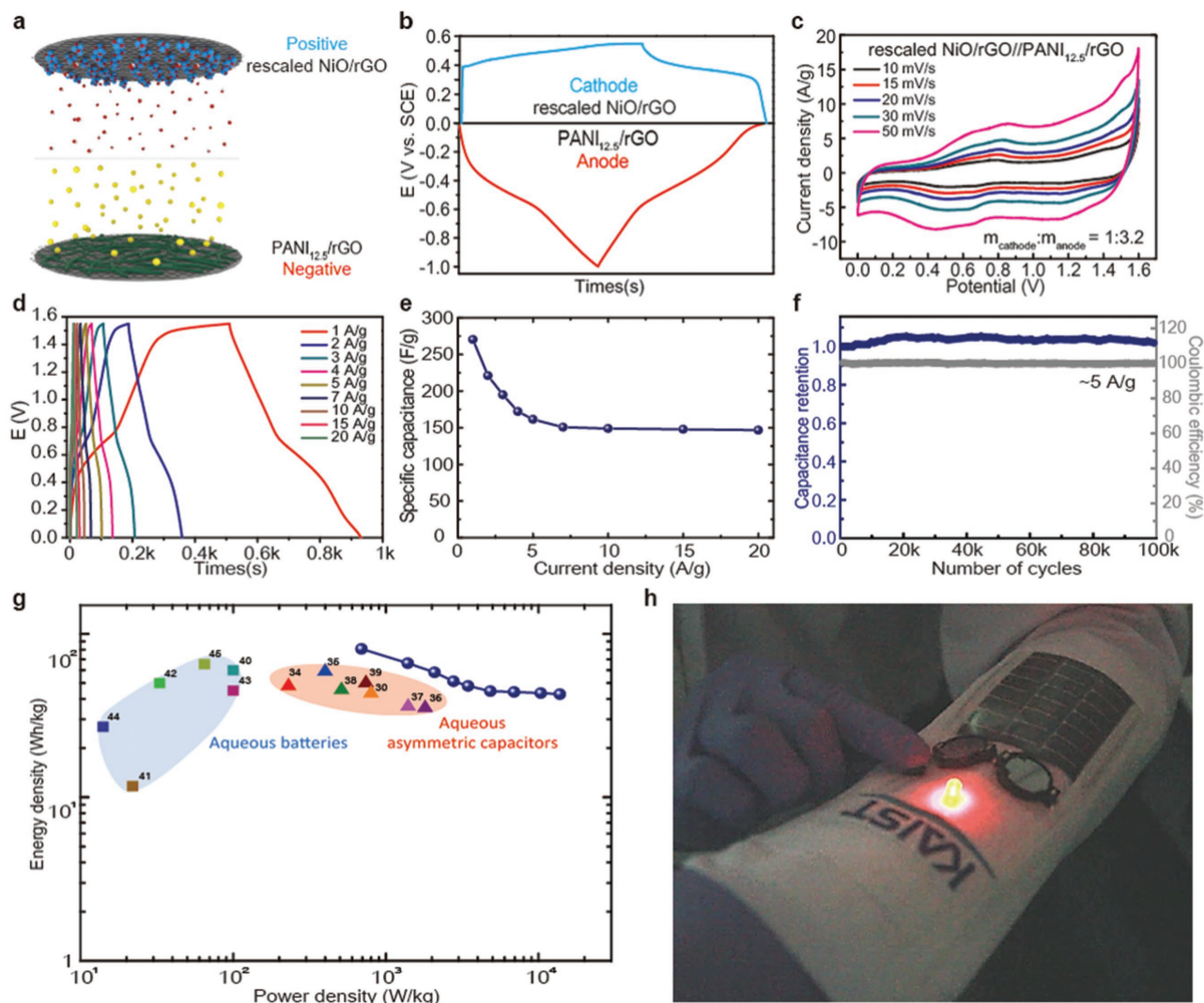

Figure 4. a) Schematic illustration of a configured AHC ($PANI_{12.5}$/rGO // rescaled NiO/rGO). Electrochemical properties of the AHC: b) Galvanostatic charge–discharge profile at potential range from 0–1.55 V, c) CV curves, d) galvanostatic charge–discharge measurements, e) gravimetric specific capacitances, f) cycling stability and Coulombic efficiency of the AHC at a current density 5 A g^{-1}, g) Ragone plots for energy storage performance of the AHC at different current densities in comparison with results of other AHCs (solid triangle plots (▲): NiO encapsulated nitrogen-rich carbon hollow porous spheres//NG,[30] $NiCo_2O_4$/rGO//HFAC,[34] NiCoAl-LDH NP/NiCo carbonate hydroxide-NW//AC,[35] $Ni(OH)_2$/CNT//rGO,[36] nanoporous Co_3O_4//AC,[37] $NiCo_2S_4$/N doped C foam//mesoporous C,[38] and NiCoS/G//porous C nanosheet,[39]) and aqueous batteries (solid square plots (■): $LiMn_2O_4$//$LiTi_2(PO_4)_3$,[40] PbO_2//AC,[41] $LiFePO_4$//$LiTi_2(PO_4)_3$,[42] CuHCF//AC/PPy,[43] CuHCF//MnHCMn,[44] and 5 M LiI//PNTCDA[45]), and h) switching wearable LED kit with two AHCs in series charged by a flexible photovoltaic module.

**ADVANCED
SCIENCE NEWS**

www.advancedsciencenews.com

**ADVANCED
ENERGY
MATERIALS**

www.advenergymat.de

peak. This demonstrates that the specific capacitance can be enhanced on the increasing active sites for atom-by-ion redox reactions. Indeed, the galvanostatic measurement at a voltage range from 0–0.55 V (Figure 3d,e; Figure S11b,c and Table S3, Supporting Information) demonstrates that the specific capacitance of 955.7 F g^{-1} for the subnanoscale NiO/rGO is obtained, which is over threefold compared to 287.2 F g^{-1} for the pristine NiO/rGO even at a current density of 1 A g^{-1}. This supports that hydroxide ions (OH$^-$) involve in atom-by-ion redox reactions with the significantly increased active sites compared to large NiO nanoparticles.

Also, the materials for anode and cathode electrodes have been assembled into a two-electrode AHC and we have measured electrochemical energy storage characteristics of the AHC in 6 M KOH aqueous electrolyte. The AHC is shown in **Figure 4**a, configured with the PANI$_{12.5}$/rGO as the anode and the rescaled NiO/rGO as the cathode. The AHC has been stably driven in a voltage range from 0 to 1.6 V, where the full operating range of the anode and cathode was utilized (Figure 4b). The AHC was assembled by adjusting the weight ratio of $m_{cathode}$:m_{anode} = 1:3.2 in order to balance the charges in anode and cathode. Two pairs of redox peaks can be identified in the overall operating voltage range of the CV curve, attributed to the pseudocapacitive anode and cathode materials (Figure 4c). The gravimetric measurements (Figure 4d,e) show that the full-cell device shows a discharge capacity of 270.1 F g^{-1} at a current density of 1 A g^{-1} at the operating voltage range. Also, the rate capability of the AHC shows the specific capacitance of 150.6 F g^{-1} at 7 A g^{-1} and the value of 146.6 F g^{-1} even at an extremely high current density of 20 A g^{-1}. The results suggest that the AHC allows sufficient redox reactions at fast charging, indicating the well-matched charge–discharge kinetic balances between anode and cathode structures. Moreover, the cycling stability of the AHC at a current density of 5 A g^{-1} (Figure 4f) demonstrates the ≈100% capacity retention and Coulombic efficiency over 100 000 redox cycles. Also, the morphology of subnanoscale NiO dispersed on the rGO in the full-cell devices has been observed by TEM analysis (Figure S12, Supporting Information) after 80 000 charge–discharge cycles, where the structure of rescaled NiO is well maintained without being agglomerated. This is also another evidence that NiO binds with the rGO via the strong NiO—C linkage after rescaling (Figure S8, Supporting Information). Figure 4g also gives a Ragone plot of the energy-storage performance of the AHC at different current densities. The AHC has the highest energy density close to 81 Wh kg^{-1}, outperforming performances of asymmetric capacitors with aqueous electrolytes[30,34–39] and aqueous batteries.[40–45] In addition, the results demonstrate that its power density of 13 794 W kg^{-1} exceeds those of aqueous batteries by about 100-folds. Indeed, two coin cells assembled in series are proven that the high power density enables ultrafast charging, as demonstrated by the flexible photovoltaic-charging wearable kit (≈20 s) and USB switching charger (≈10 s) to power a LED (Figure 4h; Figure S13 and Movies S1 and S2, Supporting Information).

In summary, we reported a new strategy to achieve high specific capacitances of both anode and cathode materials in the aqueous electrolyte. The well-conjugated PANI on rGO led to the high specific capacitance even at a high mass loading. In addition, it was discovered that reducing the size of NiO nanoparticles on graphene to subnanoscale NiO via the lithiation-induced rescaling gave enhancement in specific capacitance by about threefold. Moreover, AHCs in full-cell configurations of these polymer-based anode and subnanoscale metal oxide-based cathode, were shown to give the high energy density exceeding those of aqueous batteries, while achieving the excellent capacity retention of nearly 100% over ultralong 100 000 redox cycles. Furthermore, AHCs exhibited the high power density exceeding those of aqueous batteries by nearly 100-folds, so that AHC cells assembled in series were found to permit ultrafast charging via the flexible photovoltaic-charging wearable kit and USB switching charger. Therefore, we believe that this work would provide a new route to realize a new class of high-performance electrochemical energy storage devices by overcoming the limitations of conventional anode and cathode materials.

Supporting Information

Supporting Information is available from the Wiley Online Library or from the author.

Acknowledgements

Conflict of Interest

The authors declare no conflict of interest.

Keywords

[1] J. Yan, Q. Wang, T. Wei, Z. J. Fan, *Adv. Energy Mater.* **2014**, *4*, 1300816.
[2] J. B. Goodenough, *Energy Storage Mater.* **2015**, *1*, 158.
[3] P. Simon, Y. Gogotsi, *Nat. Mater.* **2008**, *7*, 845.
[4] Y. W. Zhu, S. Murali, M. D. Stoller, K. J. Ganesh, W. W. Cai, P. J. Ferreira, A. Pirkle, R. M. Wallace, K. A. Cychosz, M. Thommes, D. Su, E. A. Stach, R. S. Ruoff, *Science* **2011**, *332*, 1537.
[5] V. Augustyn, P. Simon, B. Dunn, *Energy Environ. Sci.* **2014**, *7*, 1597.
[6] Q. Lu, J. G. G. Chen, J. Q. Xiao, *Angew. Chem., Int. Ed.* **2013**, *52*, 1882.
[7] B. Mendoza-Sanchez, Y. Gogotsi, *Adv. Mater.* **2016**, *28*, 6104.

**ADVANCED
SCIENCE NEWS**

www.advancedsciencenews.com

**ADVANCED
ENERGY
MATERIALS**

www.advenergymat.de

[8] S. Bose, T. Kuila, A. K. Mishra, R. Rajasekar, N. H. Kim, J. H. Lee, *J. Mater. Chem.* **2012**, *22*, 767.

[9] L. W. Ji, P. Meduri, V. Agubra, X. C. Xiao, M. Alcoutlabi, *Adv. Energy Mater.* **2016**, *6*, 1502159.

[10] D. P. Dubal, O. Ayyad, V. Ruiz, P. Gomez-Romero, *Chem. Soc. Rev.* **2015**, *44*, 1777.

[11] M. H. Yu, Z. L. Wang, Y. Han, Y. X. Tong, X. H. Lu, S. H. Yang, *J. Mater. Chem. A* **2016**, *4*, 4634.

[12] W. G. Pell, B. E. Conway, *J. Power Sources* **2004**, *136*, 334.

[13] J. L. Shen, C. Y. Yang, X. W. Li, G. C. Wang, *ACS Appl. Mater. Interfaces* **2013**, *5*, 8467.

[14] Y. F. Wang, X. W. Yang, A. G. Pandolfo, J. Ding, D. Li, *Adv. Energy Mater.* **2016**, *6*, 1600185.

[15] P. Poizot, S. Laruelle, S. Grugeon, L. Dupont, J. M. Tarascon, *Nature* **2000**, *407*, 496.

[16] H. M. Jeong, K. M. Choi, T. Cheng, D. K. Lee, R. J. Zhou, I. W. Ock, D. J. Milliron, W. A. Goddard, J. K. Kang, *Proc. Natl. Acad. Sci. USA* **2015**, *112*, 7914.

[17] K. Lee, S. Cho, S. H. Park, A. J. Heeger, C. W. Lee, S. H. Lee, *Nature* **2006**, *441*, 65.

[18] S. B. Kulkarni, U. M. Patil, I. Shackery, J. S. Sohn, S. Lee, B. Park, S. Jun, *J. Mater. Chem. A* **2014**, *2*, 4989.

[19] T. Y. Liu, L. Finn, M. H. Yu, H. Y. Wang, T. Zhai, X. H. Lu, Y. X. Tong, Y. Li, *Nano Lett.* **2014**, *14*, 2522.

[20] L. M. Wang, Q. Yao, H. Bi, F. Q. Huang, Q. Wang, L. D. Chen, *J. Mater. Chem. A* **2015**, *3*, 7086.

[21] S. Golczak, A. Kanciurzewska, M. Fahlman, K. Langer, J. J. Langer, *Solid State Ionics* **2008**, *179*, 2234.

[22] P. P. Yu, Z. M. Zhang, L. X. Zheng, F. Teng, L. F. Hu, X. S. Fang, *Adv. Energy Mater.* **2016**, *6*, 1601111.

[23] K. L. Tan, B. T. G. Tan, E. T. Kang, K. G. Neoh, *Phys. Rev. B* **1989**, *39*, 8070.

[24] J. W. An, J. H. Liu, Y. C. Zhou, H. F. Zhao, Y. X. Ma, M. L. Li, M. Yu, S. M. Li, *J. Phys. Chem. C* **2012**, *116*, 19699.

[25] T. Chen, L. M. Dai, *Mater. Today* **2013**, *16*, 272.

[26] J. Chang, M. Jin, F. Yao, T. H. Kim, V. T. Le, H. Yue, F. Gunes, B. Li, A. Ghosh, S. Xie, Y. H. Lee, *Adv. Funct. Mater.* **2013**, *23*, 5074.

[27] T. Zhai, X. H. Lu, Y. C. Ling, M. H. Yu, G. M. Wang, T. Y. Liu, C. L. Liang, Y. X. Tong, Y. Li, *Adv. Mater.* **2014**, *26*, 5869.

[28] C. Guan, J. L. Liu, Y. D. Wang, L. Mao, Z. X. Fan, Z. X. Shen, H. Zhang, J. Wang, *ACS Nano* **2015**, *9*, 5198.

[29] Y. Li, J. Xu, T. Feng, Q. F. Yao, J. P. Xie, H. Xia, *Adv. Funct. Mater.* **2017**, *27*, 1606728.

[30] S. Y. Kim, H. M. Jeong, J. H. Kwon, I. W. Ock, W. H. Suh, G. D. Stucky, J. K. Kang, *Energy Environ. Sci.* **2015**, *8*, 188.

[31] X. M. Li, J. T. Zai, S. J. Xiang, Y. Y. Liu, X. B. He, Z. Y. Xu, K. X. Wang, Z. F. Ma, X. F. Qian, *Adv. Energy Mater.* **2016**, *6*, 1601056.

[32] D. Li, W. Y. Teoh, C. Selomulya, R. C. Woodward, P. Munroe, R. Amal, *J. Mater. Chem.* **2007**, *17*, 4876.

[33] G. M. Zhou, D. W. Wang, L. C. Yin, N. Li, F. Li, H. M. Cheng, *ACS Nano* **2012**, *6*, 3223.

[34] Z. Li, Z. W. Xu, H. L. Wang, J. Ding, B. Zahiri, C. M. B. Holt, X. H. Tan, D. Mitlin, *Energy Environ. Sci.* **2014**, *7*, 1708.

[35] J. Yang, C. Yu, X. M. Fan, J. S. Qiu, *Adv. Energy Mater.* **2014**, *4*, 1400761.

[36] R. R. Salunkhe, J. J. Lin, V. Malgras, S. X. Dou, J. H. Kim, Y. Yamauchi, *Nano Energy* **2015**, *11*, 211.

[37] R. R. Salunkhe, J. Tang, Y. Kamachi, T. Nakato, J. H. Kim, Y. Yamauchi, *ACS Nano* **2015**, *9*, 6288.

[38] L. F. Shen, J. Wang, G. Y. Xu, H. S. Li, H. Dou, X. G. Zhang, *Adv. Energy Mater.* **2015**, *5*, 1400977.

[39] J. Yang, C. Yu, X. M. Fan, S. X. Liang, S. F. Li, H. W. Huang, Z. Ling, C. Hao, J. S. Qiu, *Energy Environ. Sci.* **2016**, *9*, 1299.

[40] J. Y. Luo, Y. Y. Xia, *Adv. Funct. Mater.* **2007**, *17*, 3877.

[41] N. F. Yu, L. J. Gao, S. H. Zhao, Z. D. Wang, *Electrochim. Acta* **2009**, *54*, 3835.

[42] J. Y. Luo, W. J. Cui, P. He, Y. Y. Xia, *Nat. Chem.* **2010**, *2*, 760.

[43] M. Pasta, C. D. Wessells, R. A. Huggins, Y. Cui, *Nat. Commun.* **2012**, *3*, 1149.

[44] M. Pasta, C. D. Wessells, N. Liu, J. Nelson, M. T. McDowell, R. A. Huggins, M. F. Toney, Y. Cui, *Nat. Commun.* **2014**, *5*, 3007.

[45] X. L. Dong, L. Chen, J. Y. Liu, S. Haller, Y. G. Wang, Y. Y. Xia, *Sci. Adv.* **2016**, *2*, e1501038.